Investigations of Ultrafast Exciton Dynamics in Allophycocyanin Trimer†

J. M. Zhang,‡ Y. J. Shiu,§ M. Hayashi,|| K. K. Liang,‡ C. H. Chang,‡ V. Gulbinas,⊥ C. M. Yang,# T.-S. Yang,‡ H. Z. Wang,£ Yit-Tsong Chen,‡,§ and S. H. Lin*,‡,§

Institute of Atomic and Molecular Sciences, Academia Sinica, Taipei, Taiwan, ROC, Department of Chemistry, National Taiwan University, Taipei, Taiwan, ROC, Center for Condensed Matter Sciences, National Taiwan University, Taipei, Taiwan, ROC, Institute of Physics, Vilnius, Lithuania, Institute of Botany, Academia Sinica, Taipei, Taiwan, ROC, and State Key Laboratory for Ultrafast Laser Spectroscopy, Zhongshan University, Quangzhou, PRC

Received: April 4, 2001; In Final Form: June 8, 2001

The light-harvesting chromoprotein of cyanobacteria, allophycocyanin (APC), is studied both experimentally and theoretically. We observe fast kinetics and quantum beats in the pump−probe time-resolved profiles. Fourier analysis of the quantum beats provides eight vibrational frequencies: 186−215, 273−303, 352, 400, 449−469, 508, 625−664, and 840−879 cm^{-1}. We also measure anisotropy profiles which exhibit two types of kinetics; one has two fast (<1 ps) decay components, and the other almost shows no decay within 2 ps. To make use of the observed data in terms of a molecular description, the crude Born−Oppenheimer adiabatic approximation is applied to define both the electronic and vibrational states of the APC trimer. On the basis of this approximation, we construct a vibronic model, which describes the six chromophores in the APC trimer. With this molecular description, it is possible to study the steady-state optical properties and transient dynamics of the system. We analyze the absorption and CD spectra of the APC trimer, as well as oscillatory behaviors appearing in the pump−probe profiles and kinetics observed in the femtosecond anisotropy profile. We obtain a coherent set of properties of the potential energy surfaces of the system. On the basis of the vibronic model and using these molecular properties, we have simultaneously calculated the absorption and CD spectra in the spectral region 600−700 nm of the APC trimer. We have also simulated IC rate constant as a function of the electronic energy gap, electronic coupling constant, and promoting mode. Photorelated biosystems like the APC trimer may achieve an efficient IC by adjusting the electronic energy gap, promoting mode and vibronic coupling constant due to the breakdown of adiabatic approximation.

1. Introduction

Photosynthetic organisms have evolved special antenna or light-harvesting chromoprotein systems to absorb the sun's radiation energy and to transfer the captured energy efficiently to photosynthetic reaction centers, where a conversion to chemical potential energy occurs.[1] We shall study the role of chromophores in photosynthetic light-harvesting proteins by choosing the allophycocyanin (APC), an open-chain tetrapyrrole-containing protein located in the core of phycobilisome in cyanobacteria.[2] The X-ray crystal structure of the trimeric aggregation state of APC isolated from the cyanobacterium *Spirulina platensis* was recently determined by Huber and co-workers.[3] The APC trimer can be described as a C_3-symmetry, ringlike homotrimer of α- and *β*-polypeptide monomers. The phycocyanobilin chromophores (PCB) are arranged as dimers formed across the polypeptide interfaces between adjacent α- and *β*-polypeptide monomers.

APC plays a very important role in the energy transfer of blue-green algae. The structure of the APC trimer is shown in Figure 1. Figure 2 shows the absorption, fluorescence, and CD spectra of α-subunits, *β*-subunits, and APC trimers. The absorption spectrum of homogeneous monomers (not shown in the paper) is almost identical to that of α-subunits, and it has

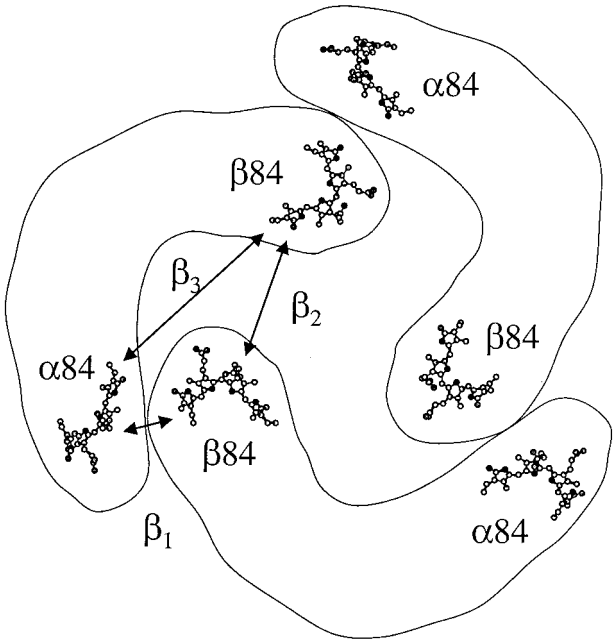

Figure 1. Schematic representation of the structure of APC trimer.

† This paper was initiallly submitted for the Edward W. Schlag Festschrift (*J. Phys. Chem. A* **2000**, no. 23, June 1, 2001).

* Corresponding author.
‡ Institute of Atomic and Molecular Sciences, Academia Sinica.
§ Department of Chemistry, National Taiwan University.
|| Center for Condensed Matter Sciences, National Taiwan University.
⊥ Institute of Physics, Lithuania.
Institute of Botany, Academia Sinica.
£ State Key Laboratory for Ultrafast Laser Spectroscopy, Zhongshan University.

10.1021/jp011266a CCC: $20.00
Published on Web 09/07/2001

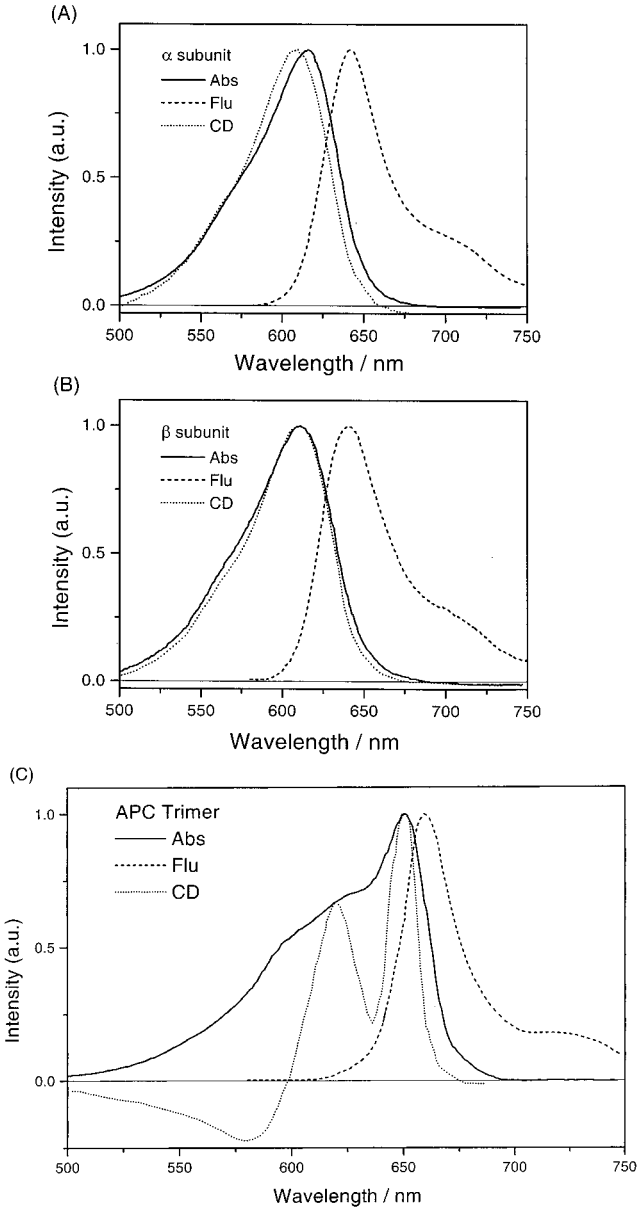

Figure 2. Observed absorption, fluorescence, and circular dichroism spectra of (a) the α-subunit, (b) the *β*-subunit, and (c) the APC trimer, at room temperature.

an absorption peak at 614 nm, while APC trimers exhibit a sharp one at 650 nm and a prominent shoulder at about 610−620 nm.

There have been two quite different proposals to explain the spectroscopic differences. The first one is that a chromophore of the monomer, either α-84 or *β*-84, is changed by interaction with apoprotein once a trimer is formed. The changed chromophore might have a unique conformation or be in different environment and possess the 650 nm peak.[3] The second proposal suggests that the two chromophores in a dimer of an APC trimer would engage in exciton splitting due to the strongly electronic coupling between them (hereafter referred as dimer model).[4−7] In the dimer model, the 650 nm peak and 610−620 nm shoulder would correspond to the two exciton states.

However, from the CD spectra of α-subunits and *β*-subunits, there is only one electronic transition involved in the wavelength range of 500−700 nm in these subunits. On the other hand, the CD spectrum of the APC trimer in the same wavelength range indicates that at least three electronic transitions exist in the APC trimer. In other words, the dimer model needs to be revised.

Recently Beck and co-workers have extensively studied transient processes of APC trimers with ultrafast femtosecond spectroscopic methods.[4−7] They have attributed the time constants of 10−60 fs to the rapid population transfer between the exciton states and the ∼220 fs component to the inter-exciton-state radiationless decay between states in either the upper exciton or lower exciton state manifolds. Such an ultrashort time constant has also been observed in other photosynthetic systems such as the reaction center (RC) and light-harvesting (LH) complexes of *Rhodobacter* (*Rb*.) *sphaeroides*.[8−14]

To interpret the origin of such ultrafast dynamics, appropriate Hamiltonian should be constructed. In other words, the nature of electronic and vibrational states involved in steady-state spectroscopy and femtosecond time-resolved profiles should be clearly defined. This is necessary especially when one discusses the nonradiative transitions among the electronic states. If electronic Hamiltonian is fully diagonalized, that is, delocalized electronic wave function is used to describe the system, nonradiative transitions between the same spin multiplicity should be driven by the breakdown of the adiabatic approximation, i.e., internal conversion (IC) process. In this case, to estimate the electronic coupling constant, Förster or Marcus type of rate constant cannot be used; i.e., the internal conversion rate constant should be used. Since IC is driven by the promoting modes, to calculate the rate constant of IC, one cannot simply use an absorption or fluorescence type of nuclear correlation functions.

Identification of electronic states of large molecular systems or assemblies such as reaction centers and light-harvesting complexes of photosynthetic bacteria is always a difficult and challenging task. One of the major reasons may be due to the fact that molecular orbital calculations for such ultralarge systems have not been quite developed yet in terms of efficiency, accuracy, and affordability, although several extensive works have been carried out quite recently.[15−23] We believe that even in the era of high-performance computers, construction of a model Hamiltonian through analyzing spectroscopic results should provide an alternative way to understand the spectroscopy and dynamics of such ultra-large systems. One of the possible requirements for a successful model Hamiltonian is that it should explain not only the observed optical spectroscopic results but also the dynamics data without modifying any part of the Hamiltonian.

The purpose of this paper is to report the femtosecond time-resolved spectroscopic measurements of APC trimers and the theoretical analysis of these experimental results. In particular, we will construct a vibronic model based on the so-called crude Born−Oppenheimer adiabatic approximation and show how the spectroscopic properties are mapped onto a model Hamiltonian. We will also show how the resulting model Hamiltonian can be used, with time-resolved spectroscopic data, to obtain internal conversion rate constant and the electronic coupling and to determine the possible promoting modes that drive the IC process. We hope this type of analysis will provide MO calculation developers with useful molecular properties for improvements of their MO methods.

In the present work, our emphasis is two-fold. First, we examine the coherence dynamics (i.e., oscillatory feature) of APC trimers. We clarify the roles of the oscillatory components appearing in pump−probe time-resolved profiles and relate them to the modes that have a significant contribution to the band-shape of the optical spectra. Second, with a vibronic model

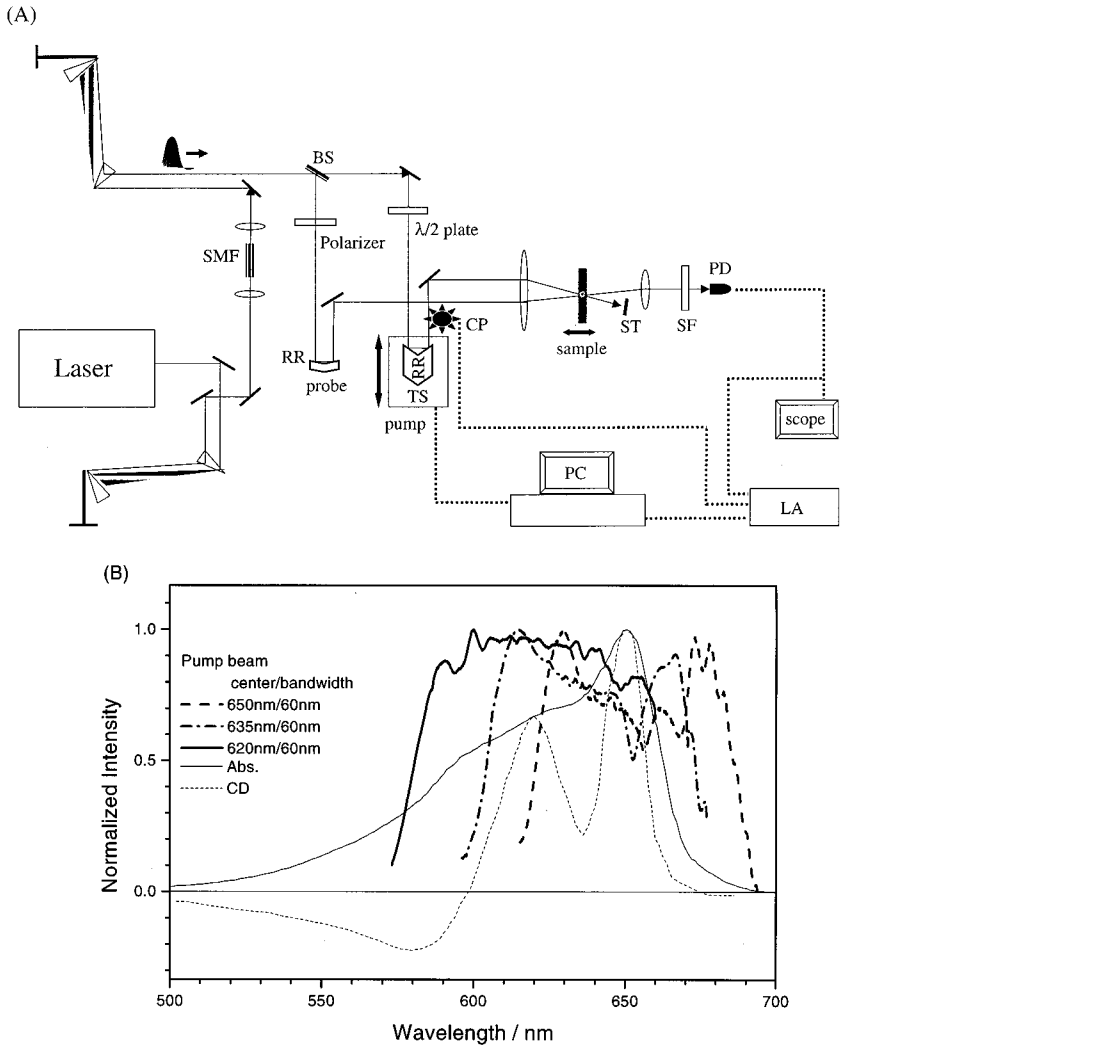

Figure 3. Pump−probe experimental setup. The details are described in the text. (A) A schematic representation of the setup; BS, beam splitter (90% T); RR, retro reflector; SF, spectral filter; SMF, single mode fiber; PD, photodiode; LA, lock-in amplifier; CP, chopper; TS, transition stage; ST, stopper. (B) Spectra of pump pulse beams centered at 650, 635, and 620 nm.

consisting of hexamer, we obtain the electronic and vibrational properties, such as the magnitudes of the interchromophore coupling that bring about such electronic energy structure and the potential energy surfaces (PESs). We will also try to justify the role of internal conversion process in the vibronic dynamics in APC trimers.

2. Experimental Setup

A schematic representation of the experimental arrangement is shown in Figure 3A. The ultrafast system was based on an optical parametric amplifier (OPA 9400, Coherent, Inc.) pumped by a Ti:sapphire laser with a regenerative amplifier (RegA 9000, Coherent, Inc.) which was pumped by a continuous-wave argon laser (Innova 400, Coherent, Inc.) and seeded by a Ti:sapphire laser (Mirra 900, Coherent, Inc.). A tunable-visible wavelength region 500−700 nm with horizontal polarization was provided by the OPA laser whose output energy was ∼250 nJ and the pulse duration time 100 fs (fwhm 6−7 nm). The repetition rate in this experiment was operated at 20 kHz. To expand the spectral bandwidth, the output pulse of the OPA laser was attenuated (15−20 nJ) and focused into a 1.5 cm fiber, and a white-light laser pulse with an fwhm of about 60 nm was generated. The energy loss within the fiber was about 50%. As shown in Figure 3A, the white light laser pulse was compressed by one pair of prisms (Fuse Silica), and the coherence time of a compressed laser pulse was obtained about 16 fs (by fitting to a sech^2 shape), as judged from autocorrelation measurements with a 0.3 mm BBO crystal at the sample position. The compressed white-light beam was split into two paths to obtain pump and probe beams with energy ratio 9:1. The pumping energy was about 3−5 nJ on average and chopped at 1 kHz. The pump and probe beams were focused into a quartz flow cell of 1 mm thickness, which contained the sample APC trimers in 100 mM buffer (sodium phosphate solution, PH 7.0). To prevent the sample from being decomposed under exposure to lights, we preserved the sample in the dark during the measurements. A band-pass filter was placed in front of a photodiode detector to select probe wavelengths. The signal was then sent to a lock-in amplifier (SRS 850) and transferred to PC.[24] Here, the delay time at the sample position between the pump and probe pulses was controlled by an optical delay line driven by a motorized translation stage. The polarizations of the pump and probe pulses were determined by a half-wave plate and a polarizer. In this experiment, we chose three pump beams whose spectra were centered at 620, 635, and 650 nm, each with fwhm 60 nm. The total of three beams covered more than half of the absorption region (500−700 nm) of the APC trimer, as shown in Figure 3B. Note that in Figure 3B, the spectrum of each pump beam is imposed on the absorption and CD spectra of the APC trimer so that one can see which spectral region is

covered under the different pump conditions. To observe the dynamics in each excited region, we monitored the probe wavelengths centered at 660, 650, 640, 630, 620, and 610 nm, each with fwhm 10 nm.

APC trimers used herein were isolated from cyanobacterium cultures of the *Anabaean variabilis*. The isolation and characterization methods for the APC trimer were described elsewhere.[25]

3. Experimental Results

The femtosecond time-resolved profiles of APC trimers at various pump and probe wavelengths were obtained, and only part of the results is shown in Figures 4 and 5. To separate nonoscillatory (DC) and oscillatory components (AC) from the observed pump−probe profiles, we used a smoothing method[26] applying a Gaussian weighting function to both weight the profiles and perform a quadratic fit.[27] For smoothing, we set a sampling proportion value to be 0.1 for a total of 256 or 512 data points. For quadratic fitting, we set the polynomial degree to 1 or 2. Frequencies involved in the AC component were extracted by fast Fourier transform method with and without singular value-decomposition procedure.[28] We also performed nonlinear fitting of the DC component to either a single- or double-exponential decay function to obtain the time constants of the kinetics. If the DC components exhibit rising components, we included in the nonlinear fitting one more function of the form $\{1 - \exp[-(t - t_0)/\tau_0]\}$ with variable amplitude.

3.1. Coherent Dynamics. Figures 4 and 5 show the pump−probe time-resolved profiles of APC trimers excited by the 650 nm pump and probed at 630 and 660 nm and those excited by the 635 nm pump and probed at 620 and 660 nm, respectively. In Figures 4A and 5A, the time-resolved profiles and the autocorrelation trace are indicated by solid and short-dotted lines, respectively. Figures 4B and 5B present the nonoscillatory and oscillatory signals extracted with the method described above. As shown in Figure 4B (5B), the transient profile probed at 630 (620) nm is characterized by decay behavior, while that at 660 (660) nm exhibits a rising feature. In other words, the nonoscillatory components in Figure 5B show time-dependent behaviors similar to those seen in Figure 4B. Figures 4C and 5C display the fast Fourier transform (FFT) power spectra with and without singular value decomposition method. In the case of the 650 nm pump and the 660 nm probe, the observed frequency components carried by quantum beats are less than 600 cm^{-1}. With the 635 nm pump, distinctive high-frequency components (>800 cm^{-1}) appear in the FFT power spectra. Since the FFT power spectra are obtained from the oscillatory parts of the experimental results, its resolution depends on the number of points of the experimental data. In this work, the resolution is within ±4.5 cm^{-1}, and thus, near the fitting error limits, the 200 and 215 cm^{-1} peaks, for example, can be considered as originating from the same vibrational mode. Table 1 summarizes the frequencies of the oscillatory components obtained in this section. At most detected wavelengths, the observed significant frequencies are 186−215, 273−303, 352, 400, 449−469, 508, 625−664, and 840−879 cm^{-1}.

3.2. Kinetics. Kinetics information can be obtained by nonlinear fitting of the nonoscillatory components that are extracted from raw data using the method described in section 3. Table 2 lists the summary of the kinetics observed in the pump−probe time-resolved profiles at magic angle with the pump wavelength centered at 635 nm. From Table 2, we can see that the nonoscillatory decay components are characterized by a slower time constant of 475−531 fs and a faster time constant of 144−181 fs. With the 660 nm probe, we observe a rising component whose characteristic time is 415 fs.

We also perform anisotropy measurements with the pump wavelength centered at 650, 635, and 620 nm. To obtain the characteristic time constants of this decay curve, we perform nonlinear fitting to a double-exponential decay function: $I(\tau) = a_0 + a_1 e^{-(t-t_0)/\tau_1} + a_2 e^{-(t-t_0)/\tau_2}$ or a single decay function: $I(\tau) = a_0 + a_1 e^{-(t-t_0)/\tau_1}$. Table 3A lists the summary of the kinetics obtained by analyzing the anisotropy profiles. Note that constant terms (a_0) are found to be more than 50% in several pump and probe conditions. In this case, it implies that much longer decay component may contribute to the profiles.

In Figure 6A, panel a shows the observed anisotropy profile with pumping at 620 nm and probing at 620 nm, while panel b exhibits that with pumping at 635 nm and probing at 660 nm. We should note here that the anisotropy kinetic shown in panel a is fit to a single-exponential decay function, and only a slow component is obtained. Similar polarization dependent measurements were carried out (one-color pump−probe at 615 nm, pulse duration 70fs) on APC trimers.[29] The characteristics of the anisotropy profile is essentially the same as that of our results. Figure 6B shows the transient profiles obtained under the parallel and perpendicular polarization conditions. The results are shown in fashion similar to that used in Figure 6A. To fit the polarization dependent profiles shown in Figure 6B, a double-exponential decay function or a single rising function $I(\tau) = a_0 + a_1(1 - e^{-(t-t_0)/\tau_1})$ is used.

Table 3B presents the time constants obtained from the polarization dependent measurement shown in Figure 6B. Notably, the kinetics of panel a in Figure 6A exhibits the slow decay component, while the corresponding polarization-dependent results show faster decay components. On the other hand, although panel b in Figure 6A shows fast decay kinetics, the corresponding polarization dependent kinetics shows fast rising components.

4. Theoretical

To analyze the spectroscopy and dynamics of APC trimers, it is obvious from the experimental results that both electronic and vibrational properties should be taken into account on equal footing. For this purpose, we will briefly introduce a molecular description of absorption spectra, circular dichroism (CD), and nonradiative electronic transitions. We will then discuss how one can construct appropriate electronic and vibrational states employing the crude Born−Oppenheimer (CBO) adiabatic approximation.

4.1. Absorption Spectra. The thermal averaged absorption coefficient can be derived using displaced potential energy surfaces with inhomogeneity in the electronic energy gap. In this case, one can define the nuclear correlation function, expressed in terms of both intramolecular and intermolecular vibrational modes. However, it is very difficult and impractical to differentiate intramolecular, low-frequency, and intermolecular vibrational modes. For this reason, we define two classes of vibrational modes as (1) high-frequency modes ($\hbar\omega_j \geq kT$, room temperature) and (2) low-frequency modes that include intramolecular, low-frequency ($\hbar\omega_j \ll kT$, room temperature), and intermolecular modes. In this case, the thermal averaged absorption coefficient of the electronic state g can be expressed as[30,31]

$$\langle \alpha(\omega) \rangle = \sum_{k=a,b,c,d,\ldots} \langle \alpha_{kg}(\omega) \rangle \qquad (1)$$

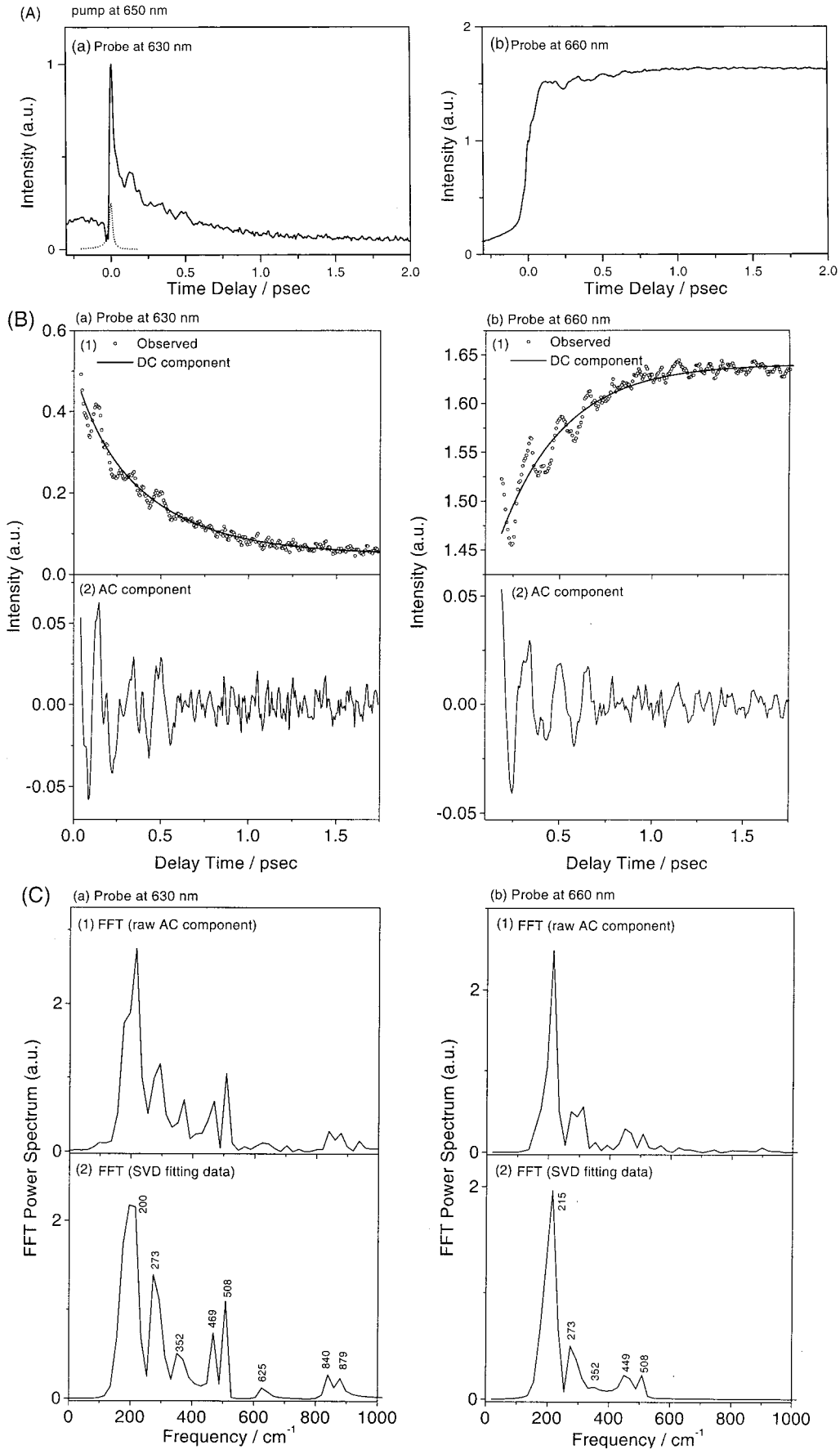

Figure 4. Observed pump−probe time-resolved profiles of APC trimer. (A) Raw data pumped at 650 nm and probed at (a) 630 and (b) 660 nm. (B) Nonoscillatory and oscillatory components are obtained by the method described in section 3. (C) Fast Fourier transform power spectra of the oscillatory components are performed (1) without and (2) with using the SVD process.

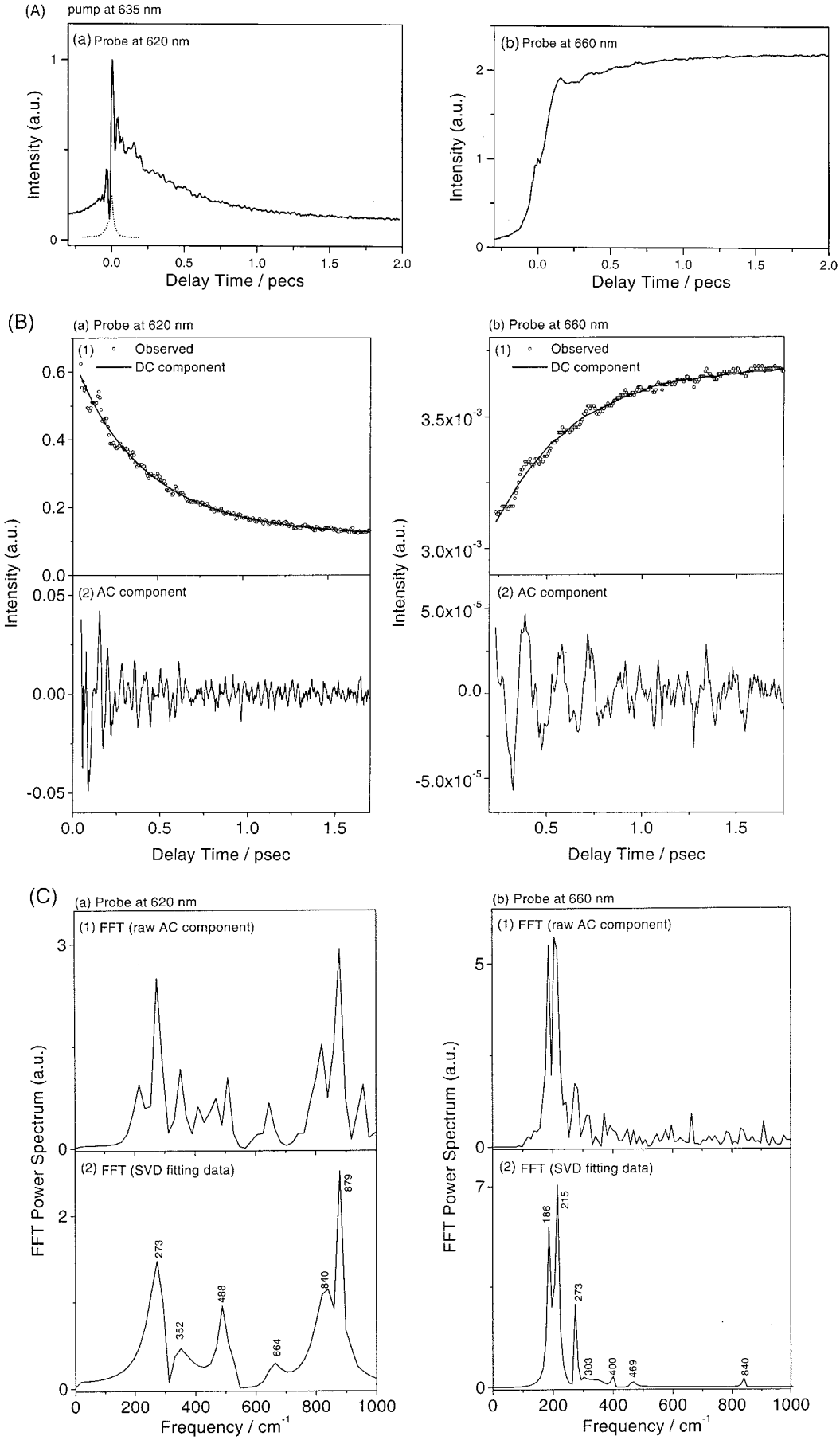

Figure 5. Observed pump−probe time-resolved spectra of APC trimer pumped at 635 nm. Panel descriptions are same as used in Figure 4.

TABLE 1: Frequencies of Oscillatory Components of APC Trimers

pump	probe	observed frequencies $\hbar\omega$/cm^{-1}
650 nm	660 nm	215, 273, 352, 449, 508
	630 nm	200, 273, 352, 469, 508, 625, 840, 879
635 nm	660 nm	186, 215, 273, 303, 400, 469, 840
	620 nm	273, 352, 488, 664, 840, 879

TABLE 2: Dynamical Information of APC Trimer at Various Probe Wavelengths at Magic Angle

pump[a]/probe[a]	t_0/fs	a_0	τ_1/fs	a_1	τ_2/fs	a_2	fitting type
635/660	233	84%	415	16%	–	–	SR[b]
635/640	53.3	25%	144	23%	531	52%	DD[c]
635/630	53.7	4%	148	21%	498	75%	DD[c]
635/620	43.3	20%	181	9%	475	71%	DD[c]

[a] In units of nm. [b] Single-exponential rising (SR): $y = a_0 + a_1\times\{1 - \exp[-(t - t_0)/\tau_1]\}$. [c] Double-exponential decay (DD): $y = a_0 + a_1\times \exp[-(t - t_0)/\tau_1] + a_2\times \exp[-(t - t_0)/\tau_2]$.

TABLE 3A: Dynamical Information of Anisotropy Profiles at Different Pump and Probe Wavelengths

pump/probe	a_0	τ_1/fs	a_1	τ_2/fs	a_2
650/660	63.8%	133	12.5%	392	23.7%
635/660	61.3%	166	17.9%	428	20.8%
635/650	47.7%	221	37.2%	870	15.1%
635/640	95.3%	576	4.70%	–	–
620/650	30.0%	327	66.2%	1360	3.80%
620/620	88.4%	2530	11.6%	–	–

TABLE 3B: Kinetics of the Time-Resolved Profiles at the Parallel and Perpendicular Polarization Conditions

polarization	a_0	τ_1/fs	a_1	τ_2/fs	a_2
	Pump/Probe 620 nm/620 nm[a]				
parallel	18.5%	192	30.0%	657	51.5%
perpendicular	18.6%	362	62.3%	1600	19.1%
	635 nm/660 nm[b]				
parallel	3.4%	477	96.6%	–	–
perpendicular	18.6%	379	81.4%	–	–

[a] $I(\tau) = a_0 + a_1 e^{-(t-t_0)/\tau_1} + a_2 e^{-(t-t_0)/\tau_2}$. [b] $I(\tau) = a_0 + a_1(1 - e^{-(t-t_0)/\tau_1})$.

where

$$\langle\alpha_{kg}(\omega)\rangle = \frac{2\pi\omega|\bar{\mu}_{kg}|^2}{3\hbar c n_e(\omega)}\int_{-\infty}^{\infty} dt\, e^{it(\omega-\bar{\omega}_{kg})-|t|\gamma_{kg}-(tD_{kg})^2/4} G_{kg}^{high}(t)G_{kg}^{low}(t) \quad (2)$$

$$G_{kg}^{high}(t) = \exp\{-\sum_j S_j[(2\bar{n}_j + 1) - (\bar{n}_j + 1)e^{it\omega_j} - \bar{n}_j e^{-it\omega_j}]\} \quad (3)$$

and

$$G_{kg}^{low}(t) = \exp\{it\lambda_{kg}^{low} - (tD_{kg}^{low})^2/4\} \quad (4)$$

Here the temperature effect is given by $\bar{n}_j = 1/[\exp(\hbar\omega_j/kT) - 1]$, ω_j stands for the vibrational frequency of the jth mode, and S_j is the coupling constant (Huang−Rhys factor) defined by $S_j = \omega_j(\Delta Q_j)^2/2\hbar$, where ΔQ_j is the difference between the minimum-energy points of the two potential energy surfaces of the electronic states k and a.

Equation 2 also contains the environmental properties (i.e., low-frequency modes): $\hbar\bar{\omega}_{kg}$ represents the averaged energy of the environmentally modified 0−0 transition energy, D_{kg} is associated with the so-called static inhomogeneity in the electronic transition energy. This inhomogeneity results from a distribution of the system−environmental electronic interactions associated with the solvation energy because various geometrical configurations of the system and environmental molecules exist in condensed phases. Here γ_{kg} is the electronic dephasing rate constant due to the interaction with the heat bath modes and photon fields.

Equation 4 shows the contribution of the low-frequency vibrational modes to the shift and broadening of the absorption spectra. These low-frequency modes can be intrachromophore and/or interchromophore (or protein) modes. It is well-known that in the high-temperature limit and the short time limit, the nuclear correlation function for such low-frequency modes approaches Gaussian form, as shown in eq 4. Here the broadening is characterized by $D_{kg}^{low} = \sqrt{\sum_i S_i\omega_i^2(2\bar{n}_i+1)}$, and the Stokes shift is given by $\lambda_{kg}^{low} = \sum_i S_i\omega_i$. The summations are carried out over low-frequency modes. To analyze the band shape of experimental absorption spectra, it should be noticed that this contribution will mix with the inhomogeneous broadening, which is represented by D_{kg}.

4.2. Circular Dichroism Spectra. Circular dichroism (CD) spectra are associated with the transition probability given by[32,33]

$$\langle\Delta W(\omega)\rangle = \sum_{k=a,b,c,d,...}\langle\Delta W_{g\to k}(\omega)\rangle \quad (5)$$

where

$$\langle\Delta W_{g\to k}(\omega)\rangle = \frac{16\pi}{3\hbar^2}\frac{8\omega^2}{c^2}|\bar{A}_0{}^0|^2\,\mathrm{Im}(\bar{\mu}_{kg}\cdot\bar{M}_{gk})\int_{-\infty}^{\infty} dt\, e^{it(\omega-\bar{\omega}_{kg})-|t|\gamma_{kg}-(tD_{kg})^2/4} G_{kg}^{high}(t)G_{kg}^{low}(t) \quad (6)$$

Here $|\bar{A}_0{}^0|^2$ is associated with the intensity of an applied field, and $\bar{M}_{gk}$ denotes the magnetic transition moment. Compared with eq 2, one can see that eq 6 is completely equivalent to eq 2 except for the coupling factors, i.e., $2\pi\omega|\bar{\mu}_{kg}|^2/3\hbar c n_e(\omega)$ in eq 2 and $(16\pi/3\hbar^2)(8\omega^2/c^2|\bar{A}_0{}^0|^2)\,\mathrm{Im}(\bar{\mu}_{kg}\cdot\bar{M}_{gk})$ in eq 6. This theoretical fact ensures that once the absorption spectrum is decomposed into several components originated from their photoinduced electronic transitions, the corresponding CD spectra can be reconstructed using these decomposed absorption components by only modifying the amplitude of each component. Equations 5 and 6 also indicate that for one electronic transition case with $\mathrm{Im}(\bar{\mu}_{kg}\cdot\bar{M}_{gk}) \neq 0$, the band shape of the CD spectrum is exactly the same as that of the absorption spectrum.

4.3. Vibronic Model. To interpret the observed steady-state spectra and the dynamical information involved in the time-resolved profiles, it is very important to determine the electronic and vibrational properties of APC trimer system. For this purpose, let us start with discussing the spectral feature of the absorption and CD spectra of subunits and trimers of APC.

The absorption and CD spectra of the α-subunit are almost identical, and those of the β-subunit are also almost identical. According to eqs 5 and 6, one optically allowed electronic transition exists within the 650−500 nm wavelength region for each subunit. In contrast, the CD spectrum of the APC trimer is quite different from its absorption spectrum, especially within the 600−700 nm region. For example, one can see two apparent peaks in the CD spectrum within this spectral region, while only one distinctive peak with a weak shoulder feature can be seen in the corresponding absorption spectrum. As mentioned in section 4.2, once the absorption spectrum is decomposed into several components originated from each photoinduced elec-

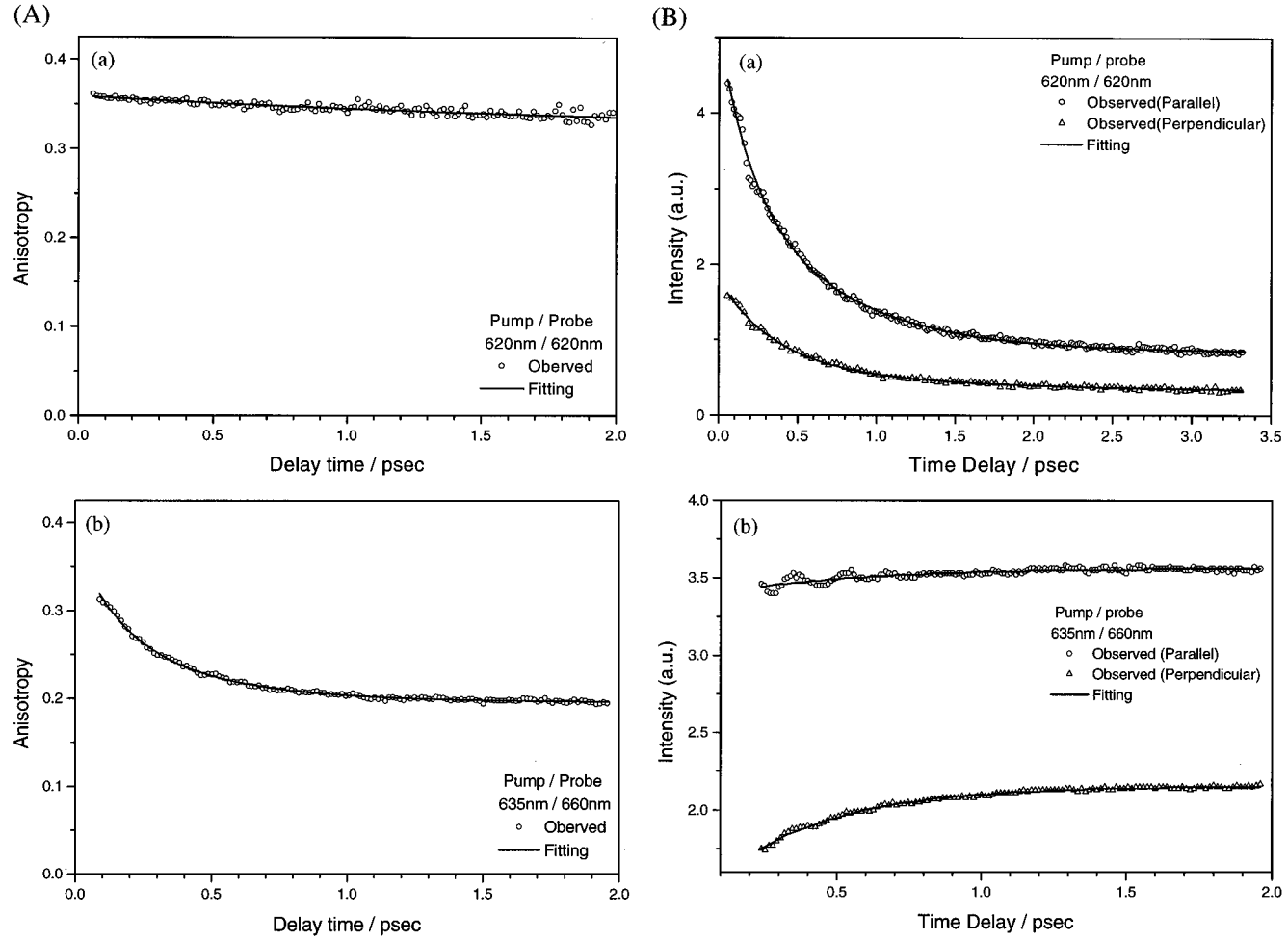

Figure 6. Observed anisotropy and polarization dependence of the pump−probe time-resolved profiles of APC trimer. Observed profiles of (A) anisotropy and (B) polarization are shown. The profiles observed different pump and probe conditions: (a) 620 nm pump and 620 nm probe and (b) 635 nm pump and 660 nm probe. Time constants of kinetics involved in the profiles are listed in Table 3.

tronic transition, the corresponding CD spectrum can be reconstructed using the resulting components by only modifying the amplitude of each component.

There has been an attempt, on the basis of a dimer model, to decompose the absorption spectrum of the APC trimer into two components.[6,7] However, the two absorption components used in the dimer model cannot explain the CD spectrum, especially within the 600−700 nm region. This situation implies that more than three electronic states exists in the 600−700 nm region. Some other possibility may also exist so that even as many as six electronic states can be involved in the steady-state spectra of the APC trimer if one takes into account the broad blue wing of the CD spectrum in the 500−600 nm range. With these considerations, we believe it necessary to consider the electronic states of a hexamer system.

On the basis of the crude Born−Oppenheimer (CBO) adiabatic approximation,[34,35] we now construct the electronic and vibrational states of the system. To simplify the discussion, we shall apply the harmonic approximation to the nuclear vibrational degrees of freedom. The essence of the CBO adiabatic approximation, in this case, can be represented by

$$\Phi_{kv}(q,Q) = [\Psi_k^{(0)}(q,0) + \Psi_k^{(1)}(q,Q) + \Psi_k^{(2)}(q,Q) + \cdots]\Theta_{kv}(Q) \quad (7)$$

where $\Psi_k^{(0)}(q,0)$ denotes the electronic wave function defined at a fixed geometry, $\Psi_k^{(1)}(q,Q)$ and $\Psi_k^{(2)}(q,Q)$ are the first and second order corrections in terms of vibronic couplings expressed by the so-called expansion parameter, respectively, and $\Theta_{kv}(Q)$ represents the a product of the harmonics oscillator wave functions of vibrational modes. Notably, $\Theta_{kv}(Q)$ is given in the zeroth order approximation, i.e., harmonic approximation.

Hereafter, we shall employ the minimum energy geometry of the electronic ground state as the fixed geometry and nuclear coordinates are defined with respect to this fixed geometry. To construct the zeroth order basis set, we shall consider a model system consisting of six chromophores, that is, three PCBs of α-subunits and tree PCBs of β-subunits. Figure 1 shows that the trimer system consists of three monomers labeled by 1, 2, and 3. In each monomer, one α-PCB and one β-PCB exist. The distance between the α- and β-PCBs of neighboring monomers is the closest among all interchromophore distances, and the second and third closest distances are, respectively, that between the α- and β-PCBs of neighboring monomers and that between the α- and β-PCBs of the same monomer. Let us now employ the localized basis set, that is

$$\psi_{\alpha_n}(q) \equiv \psi_{\alpha_n}(q,0) = \varphi_{e_{\alpha_n}}(q,0_{\alpha_n})\prod_{i\neq n}^{3}\varphi_{g_{\alpha_i}}(q,0_{\alpha_i})\prod_{j=1}^{3}\varphi_{g_{\beta_j}}(q,0_{\beta_j}) \quad (8)$$

and

$$\psi_{\beta_n}(q) \equiv \psi_{\beta_n}(q,0) = \varphi_{e_{\beta_n}}(q,0_{\beta_n})\prod_{i=1}^{3}\varphi_{g_{\alpha_i}}(q,0_{\alpha_i})\prod_{j\neq n}^{3}\varphi_{g_{\beta_j}}(q,0_{\beta_j}) \tag{9}$$

where, for example, $\varphi_{e_{\alpha_1}}(q,0_{\alpha_1})$ and $\varphi_{g_{\alpha_2}}(q,0_{\alpha_2})$ represent the first electronically excited state of the fixed geometry $\{0_{\alpha_1}\}$ and the ground electronic state of α-PCBs placed in the monomers 1 and 2, respectively. Note that $\{q\}$ denotes the electronic coordinates and $\{0\} \equiv \{\{0_{\alpha_i}\}_{i=1-3},\{0_{\beta_j}\}_{j=1-3}\}$. The total electronic Hamiltonian for the model system at the fixed geometry is then given by

$$\hat{H}_{\mathrm{el}}^{(0)} = \begin{pmatrix} \alpha & \beta_3 & 0 & \beta_1 & 0 & 0 \\ \beta_3 & \alpha' & 0 & \beta_2 & \beta_1 & \beta_2 \\ 0 & 0 & \alpha & \beta_3 & 0 & \beta_1 \\ \beta_1 & \beta_2 & \beta_3 & \alpha' & 0 & \beta_2 \\ 0 & \beta_1 & 0 & 0 & \alpha & \beta_3 \\ 0 & \beta_2 & \beta_1 & \beta_2 & \beta_3 & \alpha' \end{pmatrix} \tag{10}$$

where $\alpha = \alpha(0)$ ($\alpha' = \alpha'(0)$) denotes the energy of the first optically allowed electronic transitions of the α-PCB (β-PCB), and $\beta_1 = \beta_1(0)$, $\beta_2 = \beta_2(0)$, and $\beta_3 = \beta_3(0)$ represent the electrostatic interaction between the α- and β-PCBs of neighboring monomer, that between the α- and β-PCBs of neighboring monomer, respectively. We take into account only these three different interchromophore couplings and ignore all the other couplings because of larger distances.

Diagonalization of the Hamiltonian in eq 10 leads to the delocalized electronic states given by

$$\Psi_k^{(0)}(q,0) = c_{k_1}^{(0)}\psi_{\alpha_1}(q,0_{\alpha_1}) + c_{k_2}^{(0)}\psi_{\beta_1}(q,0_{\beta_1}) + c_{k_3}^{(0)}\psi_{\alpha_2}(q,0_{\alpha_2}) + c_{k_4}^{(0)}\psi_{\beta_2}(q,0_{\beta_2}) + c_{k_5}^{(0)}\psi_{\alpha_3}(q,0_{\alpha_3}) + c_{k_6}^{(0)}\psi_{\beta_3}(q,0_{\beta_3}) \tag{11}$$

The coefficients $\{c_{k_i}^{(0)}\}$ can be determined by solving the secular equation

$$\hat{H}_{\mathrm{el}}^{(0)}\vec{C}_k^{(0)} = \epsilon_k^{(0)}\vec{C}_k^{(0)} \tag{12}$$

where $\vec{C}_k^0 = (c_{k_1}^{(0)},c_{k_2}^{(0)},c_{k_3}^{(0)},c_{k_4}^{(0)},c_{k_5}^{(0)},c_{k_6}^{(0)})^T$.

To deal with nonradiative electronic transitions, the first-order correction should be introduced into eq 11. In this case, the interaction Hamiltonian can be defined by the difference between this Hamiltonian and the Hamiltonian defined at arbitrary geometry.

4.3. Nonradiative Transition. We have used the CBO adiabatic approximation to define the electronic and vibrational states of the APC trimer. In this scheme, all the electronic couplings are included except for the breakdown of this approximation. Thus, nonradiative electronic transitions among the electronic states with the same spin multiplicity are induced by the breakdown of the adiabatic approximation, or the so-called internal conversion mechanism. The thermal averaged rate constant for IC from the electronic states can be expressed as[36]

$$\langle W_{k\to k'}\rangle = \sum_p \frac{|R_{k'k}(p)|^2}{\hbar^2}\int_{-\infty}^{\infty} \mathrm{d}t\, \mathrm{e}^{it\bar{\omega}_{kk'}-(tD_{kk'})^2/4}F_{kk'}^p(t)G_{kk'}^{\mathrm{high}}(t)G_{kk'}^{\mathrm{low}}(t) \tag{13}$$

where $F_{kk'}^p(t)$ stands for the nuclear correlation functions for promoting modes, and they are given by[37]

$$F_{kk'}^p(t) = \frac{\omega_p}{2\hbar}\{g_+(\bar{n}_p) + S_p^{kk'}[1 + 2\bar{n}_p - g_+(\bar{n}_p)]^2\} \tag{14}$$

$$R_{kk'}(p) = -\hbar^2\left\langle \Psi_k\left|\frac{\partial}{\partial Q_p}\right|\Psi_{k'}\right\rangle_q \tag{15}$$

and

$$g_+(\bar{n}_p) = (1+\bar{n}_p)\mathrm{e}^{-it\omega_p} + \bar{n}_p\mathrm{e}^{it\omega_p} \tag{16}$$

Here ω_p stands for the vibrational frequencies of the pth promoting mode, and $S_p^{kk'}$ is its coupling constant (Huang−Rhys factor) defined by $\omega_p(\Delta Q_p^{kk'})^2/2\hbar$, where $\Delta Q_p^{kk'}$ denotes the displacement between the energy minimum positions of the potential energy surfaces of the electronic states k and k' along the normal mode p. It should be noted that the major difference between the IC rate constant and electron transfer (ET) or electronic energy transfer (EET) rate constant is due to the presence of the $F_{kk'}^p(t)$ function given in eq 14, which makes temperature dependence or the electronic-energy-gap dependence quite different from the ET (or EET) rate constant.

For the case in which the potential energy surfaces are not displaced along the normal coordinate of the promoting mode, eq 13 reduces to

$$\langle W_{k\to k'}\rangle = \sum_p \frac{|R_{kk'}(p)|^2}{\hbar^2}\frac{\omega_p(\bar{n}_p+1)}{2\hbar}\int_{-\infty}^{\infty}\mathrm{d}t\, \mathrm{e}^{it(\bar{\omega}_{kk'}-\omega_p)-|t|\gamma_{kk'}-(tD_{kk'})^2/4}G_{kk'}^{\mathrm{high}}(t)G_{kk'}^{\mathrm{low}}(t) + \sum_p \frac{|R_{kk'}(p)|^2}{\hbar^2}\frac{\omega_p\bar{n}_p}{2\hbar}\int_{-\infty}^{\infty}\mathrm{d}t\, \mathrm{e}^{it(\bar{\omega}_{kk'}+\omega_p)-|t|\gamma_{kk'}-(tD_{kk'})^2/4}G_{kk'}^{\mathrm{high}}(t)G_{kk'}^{\mathrm{low}}(t) \tag{17}$$

5. Discussions

5.1. Oscillatory Components. We have obtained several frequencies of the oscillatory components appearing in the time-resolved profiles in section 3. Some of the anisotropy profiles we obtained slightly show oscillatory features in the very early time delay region. However, we cannot assign the origin of such components to electronic coherence due to poor S/N ratios of the experimental data. Therefore, we assume that the origin of these oscillatory components observed in the time-resolved profiles (not for anisotropy) is probably due to coherent excitation of the vibrational states of APC trimers.

To theoretically construct the absorption spectrum of APC trimers, vibrational frequencies involved in the optical process should be determined. On the basis of the above observation, we choose the modes of 215, 371, 490, 742, and 879 cm^{-1} and assume that the same modes make contribution to the optical absorption in subunits. Among these modes, the 490 cm^{-1} mode is, for example, an averaged mode of 469 and 508 cm^{-1}. We did this because these two modes are only 40 cm^{-1} away from each other, and therefore, the absorption spectra analysis will not be very sensitive to the Huang−Rhys factor change of each mode if both are included. The absorption spectra of α- and β-subunits exhibit weak peak shoulders at about 1400 cm^{-1} higher-energy region from the maximum peak positions. In addition, from the resonance Raman spectroscopic study of APC trimers reported by Szaloni et al.,[38,39] many vibrational modes were found in the frequency range from ∼950 to ∼1650 cm^{-1}. Our analysis of quantum beat data can extend the vibrational

TABLE 4: Molecular Properties Obtained from Absorption Spectra Analysis

(A) Potential Energy Surface Properties for α-Subunit[a]

mode frequency(cm^{-1})	215	371	490	742	879	1400
S value	0.6	0.2	0.43	0.062	0.088	0.24

(B) Potential Energy Surface Properties for β-Subunit[b]

mode frequency (cm^{-1})	215	371	490	742	879	1400
S value	0.6	0.52	0.42	0.07	0.065	0.26

(C) Molecular Properties of APC Trimer

(a) Coupling between Subunits[c]

β_1	β_2	β_3
$-310\ cm^{-1}$	$60\ cm^{-1}$	$-30\ cm^{-1}$

(b) 0−0 Transition Energy of Exciton Levels

level	1	2	3	4	5	6
energy (cm^{-1})	15 282	15 282	15 309	15 878	15 878	16 031
oscillator strength[d] (%)	22.95	22.95	7.300	13.65	13.65	19.50
CD area (%)	20.7	20.7	48.3	1.5	1.5	7.3

(c) Potential Energy Surface Parameters

mode frequency(cm^{-1})	34[e]	83[e]	215	371	490	742	879	1400
S value (level 1−3)	0.55	0.35	0.3	0.1	0.08	0.05	0.02	0.01
S value (level 4−6)	1.6	1.1	0.3	0.1	0.08	0.05	0.02	0.01

[a] 0−0 transition energy: 15780 cm^{-1}. [b] 0−0 transition energy: 15780 cm^{-1}. [c] 0−0 transition energy: α-subunit, 15550 cm^{-1}; β-subunit, 15670 cm^{-1}. [d] See appendix A. [e] Typical protein modes,[40,41,43,44]

frequency region lower than that observed in the resonance Raman spectroscopy. In particular, such low-frequency modes information should be important for the case in which several electronic states are closely located. In this case, such low-frequency modes can assist nonradiative electronic transitions efficiently.

According to the resonance Raman analysis of APC trimers, we have chosen one high-frequency mode of 1400 cm^{-1} for analysis of both chromophore subunits and APC trimers absorption spectra. We shall also include protein modes (∼34 and ∼83 cm^{-1}) commonly observed in photosynthetic systems.[40,41] It is reported that such low-frequency modes are very important to the band shape of steady-state optical spectra.[41] In the absorption spectra analysis of both α- and β-subunits and APC trimers, we shall use this high-frequency mode, two low-frequency modes of protein modes, and the five modes mentioned above.

5.2. Absorption and CD Spectra. Several features of the spectra of the subunits, monomer, and trimer have to be discussed carefully. First, for either α- or β-subunits, the CD spectra and absorption spectra of the lowest band are almost identical, indicating that there is only one electronic state in the band. Second, the absorption spectrum of monomer (not shown) is almost identical to the that of α-subunit, while that of β-subunit is also only slightly different from it. Accordingly, we conclude that when two subunits form monomer, the spectral properties of individual subunits are not altered to any noticeable extent. The molecular properties employed in the absorption spectra analysis are listed in Table 4. Figure 7 shows the results of the theoretical calculation based on our vibronic model. Figures 7A and 7B present the calculated absorption spectra of α- and β-subunits using the molecular properties listed in Tables 4A and 4B, respectively.

According to the vibronic model for APC trimers discussed in section 4.3, it is found that, with only three nonvanishing couplings β_1, β_2, and β_3 we have chosen, there are always two pairs of doubly degenerate exciton levels. In other words, there are only four distinctive energy levels. It is interesting to find that, in the work of Csatoday et al.,[42] the absorption and CD spectra were both decomposed into four bands. Although they attributed the origin of these bands to a different model, we still find it very instructive in their fitting; namely, they have demonstrated that the absorption peaks may be clearly separated into two groups—one with much narrower band shape than the other. The coupling constants for β_1, β_2, and β_3 are listed in Table 4C-a. The coupling β_1 is found to be $-310\ cm^{-1}$. This value is compatible with the estimation of other groups. If one uses dipole−dipole interaction model to estimate these couplings, it might be expected that β_3 will be about $^1/_8$ that of $|\beta_1|$, which is roughly 39 cm^{-1}, while β_2 will be slightly larger than β_3. The values we have used are 60 cm^{-1} for β_2 and -30 cm^{-1} for β_3. Thus, these values are reasonable. For most of the pigment−protein complexes in biosystems, the couplings are always difficult to be determined from first principle. A new theoretical tool for dealing with such protein−chromophore complexes is desirable. The calculated 0−0 transition energies of the delocalized levels in the hexamer model, which are listed in Table 4C-b, are labeled in Figure 1. The six transitions form four bands because in this simple delocalized model, there are 2-folded degeneracy in the electronic transition energies. Optimization of the fitting to experimental absorption spectra are the primary criteria when we determine these values and the molecular properties needed for the absorption spectra of APC trimers are listed in Table 4C-c. Four decomposed absorption components are shown in panel a in Figure 7C. However, as the monomers gather to form trimer, the spectra are both shifted and split into several bands. This spectral change is reversible, as mentioned by Brejc[3], and we can also reproduce such a result.

According to our model calculation for the trimer, the 0−0 transition energy of α-PCB is shifted from 15780 cm^{-1} (634 nm) to 15550 cm^{-1} (643 nm), and that of β-PCB to 15670 cm^{-1} (638 nm). In our studies on other chromophore−protein complexes,[43] we found that such a spectral shift is very common, and assumption of such a shift is often necessary when a simple exciton model is employed to explain the spectral properties of these complexes. Notice that the "bare" inhomogeneous width for the chromophore units is only 20 cm^{-1}, which is small compared with β_1, β_2, and β_3. In this situation, the "bare" inhomogeneity of each chromophore is small enough to ensure the validity of the delocalized electronic state model. With the values listed in Table 4C, $\lambda_{1-3}^{low} = 47.8\ cm^{-1}$, $D_{1-3}^{low} = 141.1\ cm^{-1}$, $\lambda_{4-6}^{low} = 38.5\ cm^{-1}$, and $D_{4-6}^{low} = 126.4\ cm^{-1}$ are

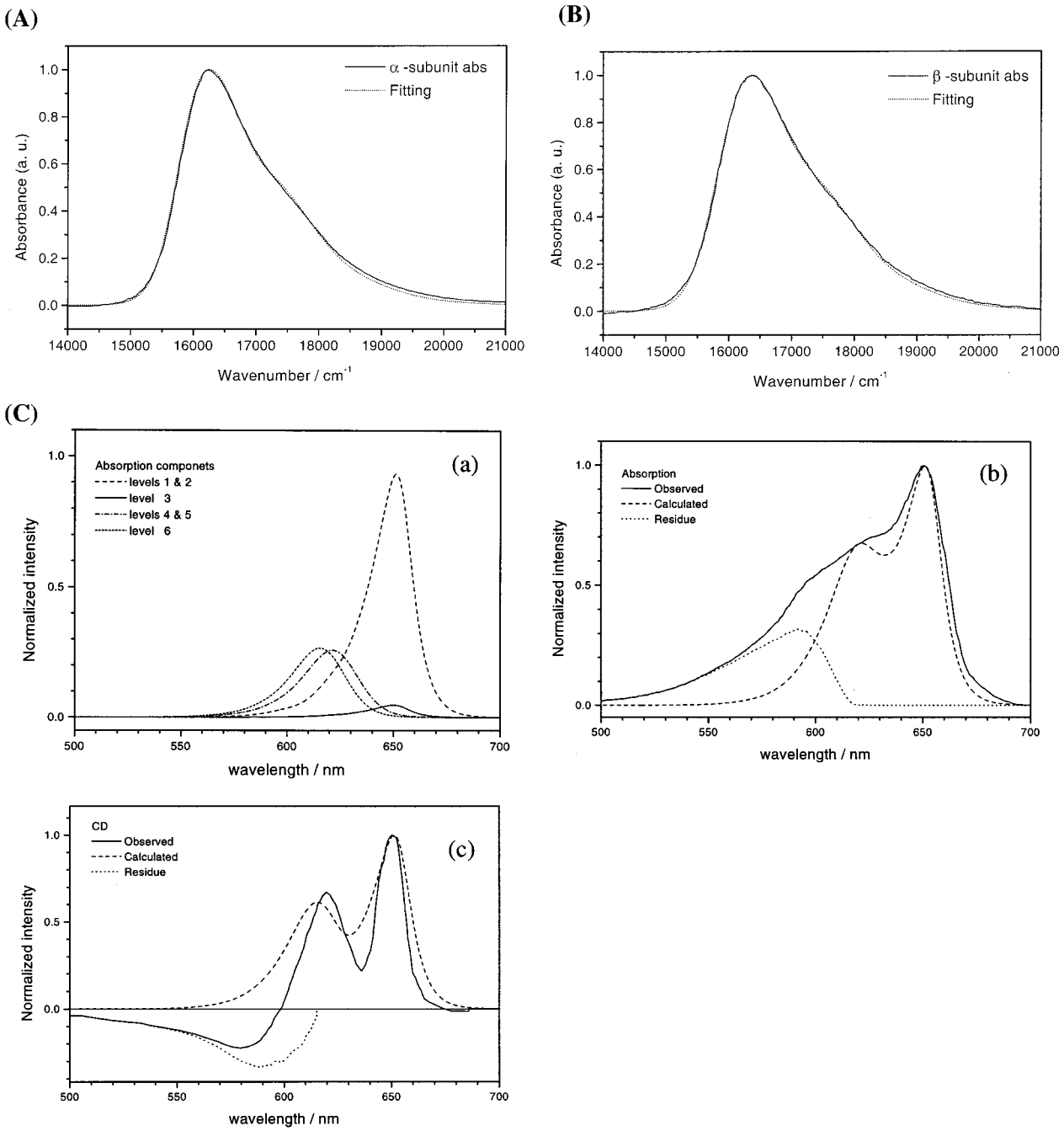

Figure 7. Calculated optical spectra of APC. The calculations are carried out for (A) the absorption spectrum of the α-subunit, (B) that of the *β*-subunit, and (C) the absorption and CD spectra of the APC trimer, at room temperature. The molecular properties used in the calculations are listed in Table 4.

obtained for the APC trimer case. These values are reasonable for photosynthetic systems.[40,44−47]

Fitting the absorption spectra and the CD spectra at the same time is a very difficult task[5] since we do not have a model for determining the magnetic transition moment between the electronic states of a PCB subunit. Moreover, according to our theory, the band shape of the absorption and CD spectra of the same transition should be the same, and of course, the 0−0 transition energy is the same. The only freedom one has is to adjust the magnitude and the sign of each CD peak. This imposes a very strict limitation on the choice of parameters. The results are listed in Table 4C-b.

We shall emphasize on the structure of the absorption and CD spectra in the range of 600−700 nm. With our hexamer model, we can construct the theoretical spectra of the hexamer assuming that six electronic states (two sets of two degenerate states and two nondegenerate states) are all located in the 600−700 nm spectral region. One can see from panels b and c in Figure 7C that the calculated absorption and CD spectra show good agreement with the observed spectra within the 600−700 nm region. In Figure 7C, we also find that the residues (620−500 nm) originating from the blue wings of the absorption and CD spectra are almost identical to each other in both position and shape. From theoretical discussion mentioned above, we assign this blue-wing residue to different electronic states that are not included in the hexamer model. It is also important to note here that the pump−probe time-resolved profiles of the 620 nm pump and the 610−580 nm probes exhibit a very fast decay component (100−200 fs) with very weak intensities (these data are not shown in this paper). On the other hand, with the

650−610 nm probes, the profiles exhibit two decay components with much stronger signal intensities, and these two components are similar to those listed in Tables 2 and 3. Moreover, in the case in which we excite much higher-energy regions with a pump pulse centered at 600 or 580 nm and probe with a probe wavelength shorter than 610 nm, we only can observe the very fast component (100 ∼ 200 fs) with very weak signal intensities. This situation implies that these kinetics result from this new band and also this new band undergoes very fast nonradiative electronic transitions.

5.3. Dynamics. In the case of ultrashort-pulse excitation, the mechanism of kinetics appearing in the transient profiles observed at magic angle could be complicated, especially for the faster dynamics because in this particular time region (100−400 fs) more than one mechanism is probably involved such as (1) destructive interference of coherently excited low-frequency modes[48,49] or the so-called Franck−Condon dynamics, (2) intramolecular vibrational redistribution,[29] (3) vibrational relaxation process due to interaction with the environment (or heat-bath modes),[29] or (4) protein matrix solvation response.[50] It may involve not only vibrational dynamics but also electronic dephasing and/or relaxation. Electronic dephasing and/or relaxation processes may occur on a time scale similar to that of the vibrational dynamics since the energy gaps of electronic states involved in 600−700 nm region (equivalent to 2381 cm^{-1}) may be smaller than 2381 cm^{-1}. In this case, internal conversion among those electronic states may occur in the femtosecond time scale. In fact, ultrafast internal conversion processes have been found within the so-called P and B bands of photosynthetic reaction centers in which the energy gap of the two electronic states in the P band region is about 893 cm^{-1} at room temperature.[41,51−54] The time constant of such processes was found to be 80−120 fs.[51−54] As have discussed so far, the time constants listed in Table 2 may represent "averaged time constant" rather than one of the possible processes. In such a case, it is important to extract the information as well as possible. Thus, we now focus on the anisotropy results.

To describe spectroscopy and dynamics of APC trimers, we have employed the CBO adiabatic approximation. In general, decay or rising components appearing in the femtosecond anisotropy profiles of very large molecular systems like photosynthetic reaction centers or APC trimers originate from the fact that photoexcitation and photoemission take place in different electronic states. This is because the time scale of rotational motion should be much slower due to the molecular weight of the system. Thus, such decay and rising components are associated with nonradiative electronic transitions. Under the CBO adiabatic approximation, nonradiative electronic transitions among the same spin multiplicity can be treated as internal conversion.

In the single promoting mode approximation, eq 17 leads to

$$\langle W_{k\rightarrow k'}\rangle = \frac{|R_{kk'}(p)|^2}{\hbar^2}\frac{\omega_p \bar{n}_p}{2\hbar}\int_{-\infty}^{\infty} dt\,[e^{it(\bar{\omega}_{kk'}-\omega_p)} + e^{it(\bar{\omega}_{kk'}+\omega_p)}]e^{-|t|\gamma_{kk'}-(tD_{kk'})^2/4}G_{kk'}^{high}(t)G_{kk'}^{low}(t) + \frac{|R_{kk'}(p)|^2}{\hbar^2}\frac{\omega_p}{2\hbar}\int_{-\infty}^{\infty} dt\, e^{it(\bar{\omega}_{kk'}-\omega_p)-|t|\gamma_{kk'}-(tD_{kk'})^2/4}G_{kk'}^{high}(t)G_{kk'}^{low}(t) \quad (18)$$

Here the right-hand-side of eq 18 is a function of the vibrational properties of the promoting modes and accepting modes, the energy gap between the electronic states k and k', the electronic coupling matrix element $R_{kk'}(p)$ induced by the promoting modes, and the static inhomogeneous broadening $D_{kk'}$. Once the values of $D_{kk'}$, $\langle W_{k\rightarrow k'}\rangle$, and the vibrational properties except for the promoting modes are substituted into eq 18, we notice that this equation can provide possible combinations of the values of $R_{kk'}(p)$ and ω_p at a given electronic gap $\hbar\bar{\omega}_{kk'}$.

From the spectroscopic analysis and using our vibronic model in Table 4C-b, there are six possible energy gaps between two electronic states, and they are given by 27, 153, 569, 596, 722, and 749 cm^{-1}, respectively. As listed in Table 3A, several time constants are observed in the anisotropy kinetics depending on the pump and probe conditions, and they can be grouped into two groups 133, 166, and 221 fs and (2) 327, 392, 428, and 576 fs. We ignore the decay component slower than 1 ps. For simplicity, we average these time constants within the same group and obtain (1) 173 and (2) 430 fs. From this consideration, we know the values of $\langle W_{k\rightarrow k'}\rangle$. For $D_{kk'}$ and the vibrational modes except for the promoting modes, we can adopt the necessary values from the analyzed results of the absorption and CD spectra of ACP trimers.

Let us now consider a single promoting mode case for treating the slower IC case, i.e., 430 fs. We assume that the slower IC takes place between the electronic states of the largest energy gap. From eq 18, in this case, $|R_{kk'}(p)|/2\pi c\hbar^3$ can vary from 85.8 to 142 cm^{-1} with a promoting mode less than 585 cm^{-1}. These coupling constant and promoting mode ranges are reasonable compared with photosynthetic reaction centers.[43] If a different energy gap, for example, 596 cm^{-1}, is chosen, these ranges will be 102−123 cm^{-1} for $|R_{kk'}(p)|/2\pi c\hbar^3$, and $\hbar\omega_p$ will be less than 430 cm^{-1}. Thus, for the slower IC, APC systems may easily achieve a possible combination of the electronic energy gap, the promoting mode, and vibronic coupling constant even for the single promoting case.

For the faster IC case, we find that the range of $|R_{kk'}(p)|/2\pi c\hbar^3$ shifts to a higher-energy region, and the minimum value of $|R_{kk'}(p)|/2\pi c\hbar^3$ is as large as 213 cm^{-1}. This value is almost twice as large as that in the case of the reaction centers. This situation implies that more than one promoting mode may contribute to this IC. Or it may also be due to the fact that electronic coherence between the electronic states with the lowest energy gap (such as 27 or 153 cm^{-1}) generated by a pump process is rapidly thermalized via dephasing processes. To clarify the origin of the faster component, detailed analysis is be needed.

6. Conclusion

We have analyzed the absorption, fluorescence, CD spectra, and pump−probe time-resolved profiles of the APC trimer system at room temperature. To understand these spectra, we have employed the CBO adiabatic approximation and proposed a vibronic model consisting of six subunits. In this approximation, one can treat the electronic and vibrational states on equal footing. To obtain the vibrational information on the excited states, we have performed femtosecond pump−probe time-resolved measurements on this system and observed quantum beats that are originated from coherent vibration motion of this system. Probing wavelength-dependent quantum beats provide several vibrational frequencies, and we find that six of them are persistent, 215, 371, 490, 742, 879, and 1400 cm^{-1}. Assuming that these modes are responsible for the absorption spectra, using the vibronic model, we have calculated the absorption spectra, which show good agreement with the observed ones.

Nonoscillatory components of quantum beat signals provide additional information about ultrafast dynamics of the APC

trimer system. We have found that the nonoscillatory components can be characterized by one or two decay components. For one decay component case, the time constant is within 415−531 fs, while for two decay components case, we find an additional fast time constant of 132−144 fs. To isolate information, we have also performed anisotropy measurements and found two group of transient processes (1) 133−221 fs and (2) 327−576 fs in the anisotropy profiles. We have assigned that the slower time constants result from internal conversion among the electronic states proposed by using the CBO adiabatic approximation. We have shown, using eq 18, that it is possible for APC trimers to achieve an appropriate combination of $\hbar\omega_p$, $|R_{kk'}(p)|/2\pi c\hbar^3$, and $\hbar\bar{\omega}_{kk'}$. On the other hand, we feel that the origin of the faster components observed in the anisotropy profiles may be complicated. To understand the mechanism of the faster components, a more detailed analysis should be performed.

Appendix

A. Transition Dipole Moments in Terms of CBO Basis Set. To treat optical transitions originated from the electronic ground state, we assume the Condon approximation which corresponds to the zeroth-order CBO approximation. In the Condon approximation, the electronic transition moment between

$$\Psi_k^{(0)}(q,0) \quad \text{and} \quad \Psi_g^{(0)}(q,0) = \prod_{i=1}^{3}\varphi_{g_{\alpha_i}}(q,0_{\alpha_i})\prod_{j=1}^{3}\varphi_{g_{\beta_j}}(q,0_{\beta_j})$$

is given by

$$\begin{aligned}\bar{\mu}_k &= \langle\Psi_k^{(0)}|\sum_{i=1}^{3}\bar{\mu}(\alpha_i) + \sum_{j=1}^{3}\bar{\mu}(\beta_j)|\Psi_g^{(0)}\rangle_q \\ &= c_{k_1}^{(0)}\bar{\mu}_{\alpha_1} + c_{k_2}^{(0)}\bar{\mu}_{\beta_1} + c_{k_3}^{(0)}\bar{\mu}_{\alpha_2} + c_{k_4}^{(0)}\bar{\mu}_{\beta_2} + \\ &\qquad c_{k_5}^{(0)}\bar{\mu}_{\alpha_3} + c_{k_6}^{(0)}\bar{\mu}_{\beta_3} \quad \text{(A1)}\end{aligned}$$

where $\langle|\cdots|\rangle_q$ stands for integral taking over the electronic coordinates $\{q\}$ and $\bar{\mu}_{\alpha_1} = \langle\psi_{e_{\alpha_1}}|\bar{\mu}(\alpha_1)|\psi_{g_{\alpha_1}}\rangle_q$, for example, represents the electronic transition dipole moment of the α-PCB in the monomer 1. The oscillator strength of the kth electronic state is proportional to $|\bar{\mu}_k|^2$. The calculation of $|\bar{\mu}_k|^2$ requires the inner product of the electronic transition dipole moments of α- and β-PCBs; in other words, all the orientations of the six electronic transition dipole moments are needed.

Brejc and co-workers have summarized the X-ray crystal structure of APC trimer.[3] The relative positions and orientations of the chromophores were listed. In their work, the orientation of the transition moment of each chromophore is approximated by a line fitted to the conjugated π-electron system of the chromophore. The relative positions are the coordinates of the centers of gravity of these chromophores in certain laboratory-fixed coordinates. The actual orientations of the transition moments are certainly not perfectly parallel to the orientation given in this work. However, we assumed that the actual transition dipole in each chromophore makes the same relative angle to the molecular orientation they obtained. With these assumptions on the transition dipole orientation, we can calculate the 0−0 transition energy as well as the oscillator strength of all six exciton levels.

B. Single-Vibronic Nonradiative Transition Rate Constant. For the case in which the time-resolved profiles exhibit oscillatory behavior, that is, the excited state prepared via the pumping pulse is not vibrationally relaxed, an appropriate description of internal conversion rate should be the single vibronic transition rate constant:

$$\langle W_{k\{\nu\}}\rangle = \sum_{\{\nu'\}}\langle W_{k\{\nu\}\to k'\{\nu'\}}\rangle \quad \text{(B1)}$$

where

$$\begin{aligned}\langle W_{k\{\nu\}\to k'\{\nu'\}}\rangle = \frac{2\pi|R_{kk'}|^2}{\hbar}\left|\left\langle\chi_{k\nu_p}\left|\frac{\partial}{\partial Q_p}\right|\chi_{k'\nu'_p}\right\rangle\right|^2 \\ \prod_{j\neq p}|\langle\chi_{k\nu_j}|\chi_{k'\nu'_j}\rangle|^2\langle D(E_{k\{\nu\}} - E_{k'\{\nu'\}})\rangle \quad \text{(B2)}\end{aligned}$$

Here $\langle D(E_{k\{\nu\}} - E_{k'\{\nu'\}})\rangle$ denotes the band-shape function and is given by

$$\langle D(E_{k\{\nu\}} - E_{k'\{\nu'\}})\rangle = \int_{-\infty}^{\infty} \mathrm{d}t\, \mathrm{e}^{it[\bar{\omega}_{kk'} + \sum_l(\nu_l - \nu'_l)\omega_l] - |t|\gamma_{kk'} - (tD_{kk'})^2/4} \quad \text{(B3)}$$

By substituting the vibrational wave functions of the displaced harmonic potential model into eq B2, the rate constant $W_{k\nu}$ is given by

$$\begin{aligned}\langle W_{k\{\nu\}}\rangle = \frac{2\pi|R_{kk'}|^2}{\hbar}\left(\frac{\omega_p}{2\hbar}\right)\sum_{\nu'_p}[\nu'_p|\langle\chi_{k\nu_p}|\chi_{k'\nu'_p-1}\rangle|^2 + \\ (\nu'_p+1)|\langle\chi_{k\nu_p}|\chi_{k'\nu'_p+1}\rangle|^2]\prod_{j\neq p}\sum_{\nu_j}|\langle\chi_{k\nu_j}|\chi_{k'\nu'_j}\rangle|^2 D(E_{k\{\nu\}} - E_{k'\{\nu'\}}) \quad \text{(B4)}\end{aligned}$$

where the overlap integral can be expressed as

$$\langle\chi_{k\nu}|\chi_{k'\nu'}\rangle = \mathrm{e}^{-S/2}\sum_{m=0}^{\nu}\sum_{n=0}^{\nu'}(-1)^m\frac{\delta_{\nu-m,\nu'-n}}{m!n!}\sqrt{\frac{\nu!\nu'!S^mS^n}{(\nu-m)!(\nu'-n)!}} \quad \text{(B5)}$$

Here $\delta_{\nu-m,\nu'-n}$ denotes the Kronecker delta function.

Acknowledgment. The authors wish to thank the Nan Pao Resins Chemical Co., Ltd. Bio. Department in Tainan, Taiwan, for providing us with cyanobacteria for preparation of the APC sample. The authors also wish to thank the referees for helpful suggestions and discussions. Y.J.S. would like to thank Dr. C. H. Lee, Prof. T. P. Wang, and his group for providing advice on the laser system and optics. This work was financially supported by NSC of ROC, NSFC of PRC, and Academia Sinica of ROC.

References and Notes

(1) Holzworth, A. Quart. *Rev. Biophys.* **1989**, *22*, 239.
(2) Glazer, A. N. *Annu. Rev. Biophys. Chem.* **1985**, *14*, 47.
(3) Brejc, K.; Ficner, R.; Huber, R.; Steinbacher, S. *J. Mol. Bio.* **1995**, *249*, 424.
(4) Edington, M. D.; Riten, R. E.; Beck, W. F. *J. Phys. Chem.* **1995**, *43*, 15769.
(5) Edington, M. D.; Riter, R. E.; Beck, W. F. *J. Phys. Chem.* **1996**, *100*, 14206.
(6) Edington, M. D.; Riter, R. E.; Beck, W. F. *J. Phys. Chem. B* **1997**, *101*, 4473.
(7) Homoelle, B. J.; Edington, M. D.; Diffey, W. M.; Beck, W. F. *J. Phys. Chem. B* **1998**, *102*, 3044.
(8) Jimenez, R.; van Mourik, F.; Yu, J. Y.; Fleming, G. R. *J. Phys. Chem. B* **1997**, *101*, 7350.
(9) Jimenez, R.; Dikshift, S. N.; Bradforth, S. E.; Fleming, G. R. *J. Phys. Chem.* **1996**, *100*, 6825.

(10) Bradforth, S. E.; Jimenez, R.; van Mourik, F.; van Grondelle, R.; Fleming, G. R. *J. Phys. Chem.* **1995**, *99*, 16179.
(11) Jia, Y.; Jonas, D. M.; Joo, T.; Nagasawa, Y.; Lang, M. J.; Fleming, G. R. *J. Phys. Chem.* **1995**, *99*, 6263.
(12) Wynne, K.; Haran, G.; Reid, G. D.; Moser, C. C.; Dutton, P. L.; Hochstrasser, R. M. *J. Phys. Chem.* **1996**, *100*, 5140.
(13) Walker, G. C.; Maiti, S.; Cowen, B. R.; Moser, C. C.; Dutton, P. L.; Hochstrasser, R. M. *J. Phys. Chem.* **1994**, *98*, 5778.
(14) Arnett, D. C.; Moser, C. C. Dutton, P. L.; Scherer, N. F. *J. Phys. Chem. B* **1999**, *103*, 2014.
(15) Scholes, G. D.; Harcourt, R. D.; Fleming, G. R. *J. Phys. Chem. B* **1997**, *101*, 7302.
(16) Thompson, M. A.; Zerner, M. C. *J. Am. Chem. Soc.* **1991**, *113*, 8210.
(17) Thompson, M. A.; Zerner, M. C.; Fajer, J. *J. Phys. Chem.* **1991**, *95*, 5693.
(18) Parson, W. W.; Warshel, A. *J. Am. Chem. Soc.* **1987**, *109*, 6143.
(19) Scherer, P. O. J.; Fischer, S. F. *Chem. Phys*. **1989**, *131*, 115.
(20) Scherer, P. O. J.; Fischer, S. F.; Lancaster, C. R. D.; Fritzsch, G.; Schmidt, S.; Arlt, T.; Dressler, K.; Zinth, W. *Chem. Phys. Lett.* **1994**, *223*, 110.
(21) Scherer, P. O. J.; Scharnagl, C.; Fischer, S. F. *Chem. Phys.* **1995**, *197*, 333.
(22) Scherer, P. O. J.; Fischer, S. F. *Chem. Phys. Lett.* **1997**, *268*, 133.
(23) Scherer, P. O. J.; Fischer, S. F. *Spectrochim. Acta, Part A* **1998**, *54*, 1191.
(24) Yang, T.-S.; Chang, M.-S.; Chang, R.; Hayashi. M.; Lin, S. H.; Vohringer, P. Dietz, W.; Schere, N. F. *J. Chem. Phys.* **1999**, *110*, 12070.
(25) Zhang, J. M.; Zhao, J, Q.; Jiang, L. J. *Photochem. Phtobiol.* **1998**, *68*, 777.
(26) Press, W. H.; Teukolsky, S. A.; Vettering, W. T.; Flannery, B. P. *Numerical Recipes*, 2nd ed.; Cambridge University Press: New York, 1992.
(27) Wang, S. S. *Computational Methods in Physics and Engineering*, 2nd ed.; World Scientific: Singapore, 1997.
(28) Naidu, P. S. *Modern Spectrum Analysis of Time Series*; CRC Press: New York, 1995.
(29) Sharkov, A. V.; Kryukov, I. V.; Khoroshilov, E. V.; Kryukov, P. G.; Fischer, H.; Gillbro, T. *Biochim. Biophys. Acta* **1994**, *1188*, 349.
(30) Lin, S. H.; Hayashi, M.; Alden, R. G.; Suzuki, S.; Gu, X. Z.; Lin, Y. Y. In *Femtosecond Chemistry*; Mantz, J., Wöste, L., Eds.; VCH: New York, 1995; p.633.
(31) Lin, S. H.; Hayashi, M.; Suzuki, S.; Gu, X. Z.; Xiao, W.; Sugawara, M. *Chem. Phys.* **1995**, *197*, 433.
(32) Lin, S. H. *J. Chem. Phys.* **1971**, *54*, 1177.
(33) Lin, S. H. *J. Chem. Phys.* **1971**, *55*, 3546.
(34) Born, M.; Huang, K *Dynamical Theory of Crystal Lattices*; Oxford University Press: Oxford, 1954; Chapter IV.
(35) Ballhausen, C. J.; Hansen, A. E. *Annu. Rev. Phys. Chem.* **1972**, *23*, 15.
(36) Lin, S. H. *J. Chem. Phys.* **1966**, *44*, 3759.
(37) Mebel, A.; Hayashi, M.; Liang, K. K.; Lin, S. H. *J. Phys. Chem. A* **1999**, *103*, 10674. See Appendix D.
(38) Szalontai, B.; Gombos, Z.; Gsizmadia, V.; Castorday, K.; Lutz, M. *Biochemistry* **1989**, *28*, 6467.
(39) Szalontai, B.; Gombos, Z.; Gsizmadia, V.; Bugyinka, C.; Lutz, M. *Biochemistry* **1994**, *33*, 11823.
(40) Lyle, P. A.; Kolaczkowski, S. V.; Small, G. J. *J. Phys. Chem.* **1993**, *97*, 6924.
(41) Chang, C. H.; Hayashi, M.; Chang, R.; Liang, K. K.; Yang, T. S.; Lin, S. H. *J. Phys. Chem. B* **2001**, *105*, 1216.
(42) Csatorday, K.; MacColl, R.; Csizmadia, V.; Grabowski, J.; Bagyinka, C. *Biochemistry* **1984**, *23*, 6466.
(43) Chang, C.-H.; Hayashi, M.; Chang, R.; Liang, K. K.; Yang, T.-S.; Lin, S. H. *J. Chin. Chem. Soc.* **2000**, *47*, 785.
(44) Small, G. J. *J. Chem. Phys.* **1995**, *197*, 239.
(45) Tang, D.; Jankowiak, R.; Small, G. J.; Tiede, D. M. *Chem. Phys.* **1989**, *131*, 99.
(46) Pieper, J.; Voigt, J.; Small, G. J. *J. Phys. Chem. B* **1999**, *103*, 2319.
(47) Reddy, N. R. S.; Wu, H.-M.; Jankwoiak, R.; Picorel, R.; Cogdell, R. J.; Small, G. J. *Phytosynth. Res.* **1996**, *48*, 277.
(48) Joo, T.; Jia, Y.; Yu, J.-Y.; Lang, M. J.; Fleming, G. R. *J. Chem. Phys.* **1996**, *104*, 6089.
(49) Fleming, G. R.; Cho, M. *Annu. Rev. Phys. Chem.* **1996**, *47*, 109.
(50) Riter, R. E.; Edington, M. D.; Beck, W. F. *J. Phys. Chem.* **1996**, *100*, 14198.
(51) Wynne, K.; Haran, G.; Reid, G. D.; Moser, C. C.; Dutton, P. L.; Hochstrasser, R. M. *J. Phys. Chem.* **1996**, *100*, 5140.
(52) Haran, G.; Wynne, G. D.; Moser, C. C.; Dutton, P. L.; Hochstrasser, R. M. *J. Phys. Chem.* **1996**, *100*, 5562.
(53) Jonas, D. M.; Lang, M. J.; Nagasawa, Y.; Joo, T.; Fleming, G. R. *J. Phys. Chem.* **1996**, *100*, 12660.
(54) Arnett, D. C.; Moser, C. C.; Dutton, P. L.; Scherer, N. F. *J. Phys. Chem. B* **1999**, *103*, 2014.